Morphology modulated brookite TiO₂ and BaSnO₃ as alternative electron transport materials for enhanced performance of carbon perovskite solar cells

Shubhranshu Bhandari [a,*], Anurag Roy [a], Tapas Kumar Mallick [a], Senthilarasu Sundaram [b,*]

[a] Environment and Sustainability Institute (ESI), Penryn Campus, University of Exeter, Cornwall TR10 9FE, UK
[b] Electrical and Electronics Engineering, School of Engineering and the Built Environment, Edinburgh Napier University, Edinburgh EH10 5DT, UK

ABSTRACT

Designing alternatives to TiO₂ electron-transport layers (ETLs) for facile electron extraction and transport to enhance the efficiency of n-i-p structured carbon perovskite solar cells (CPSC) is still a less explored research interest. In this work, the combined effect of the phase and morphology of BaSnO₃ (BSO) and brookite TiO₂ (BTO) nanostructured materials are explored as alternative electron transport layers (ETLs) instead of dominating anatase TiO₂ in CPSC. The highest power-conversion efficiencies (PCEs) of CPSCs with rod-shaped BTO and BSO were recorded at ~15.02% and ~13.4%, respectively, which claims the highest efficiency for BTO and BSO CPSCs in ambient conditions to the best of our knowledge. In addition, our findings indicate that the CPSC's with rod structured BTO and BSO exhibited decreased charge recombination and improved efficiency compared to concerning spherical morphologies (12.5% for BSO nanoparticles) and cubic particles (14% for BTO nanocubes) due to the superior photogenerated charge-carrier extraction and enhanced interface quality. This research will open the door for various morphologies of alternative ETL materials and their physicochemical understanding toward achieving high-efficiency ambient CPSCs.

1. Introduction

Solar energy, as an integral part of renewable energy, can be one of the most valuable contributors to future energy management. As the fastest developing technology in the history of photovoltaics (PV), halide perovskite solar cells (PSCs) have manifested a rapid rise in power conversion efficiency (PCE) from 3.8% to a certified value of >25% [1–6]. In addition to the high PCE, the lifetime (stability) has become a new goal for the expeditious development of perovskite-based optoelectronic devices [7–10]. There are mainly two categories of the stability issues such as environmental or extrinsic factors and intrinsic factors [11,12]. Extrinsic factors such as light, heat, moisture, and oxygen can cause the degradation of the halide perovskite photoactive materials into their non-photoactive state [13,14]. The defect states in the perovskite materials and the interfacial contacts between charge transport layers (CTLs) and perovskites, on the other hand, hold the key to intrinsic stability [15,16]. Thermal instability of halide perovskites, ion migration, and hygroscopic nature of organic cations are the main intrinsic features responsible for perovskite instability [17,18]. In this

regard, encapsulation of devices can solve the hygroscopicity problem and all-inorganic perovskite devices via compositional engineering can be effective for thermal stress [19,20]. Again, the implementation of carbon-based top electrodes enhances hygroscopic stability maintaining a low-cost fabrication process that draws the researcher's attention in developing large-scale carbon perovskite solar cells (CPSC) [21–25]. On the other hand, the migration of ions can be controlled by grain boundary passivation through interfacial engineering, which in turn improves the performance of devices, improving the charge transfer process [26–28]. Traditionally, anatase TiO₂ has been used as electron transport material (ETM), although sometimes this device architecture suffers due to the carrier transport property and electron mobility of anatase TiO₂ [29]. Deploying various interfacial modification techniques like alkali doping, solvent engineering and tuning particle nature, significant improvements of PCE and stability have been achieved for anatase TiO₂ based devices in recent years [30–32]. In addition, several other materials like ZnO, CeOₓ, SnO₂ etc., have been utilized as the electron transport layer (ETL), and among them, BaSnO₃ (BSO) and brookite TiO₂ (BTO) have shown significant results [33–40]. Structural

modification or change of phase of the same material has already proven very effective in different fields of materials science due to less defect states or grain boundary traps [41–43]. BTO and anatase TiO_2 are polymorphs of each other, although parameters like density and distribution of the trap states, electron mobility, and the electron transfer rate constant make them distinguishable from each other [44]. In fact, reports suggest that the PCE and stability of BTO based devices achieved better results compared to the anatase TiO_2 based devices having the same architecture [45]. On the other side, BSO, due to its relatively high band-gap, electron mobility, easily modifying nature via doping, has proven its capability as ETM [39,46]. In this regard, particle size and morphology of the materials, as mentioned earlier, play a crucial role in their application for PSCs. To date, only a few works have been done using various morphologies of the BSO and BTO for PSC and hardly any for carbon electrode-based devices. In this regard finding out the combined effect of phase and morphology can be a game-changer for CPSC in ambient conditions.

Here, we considered different morphology of synthesized single-phase BSO and BTO nanostructures as ETL for the ambient CPSC, which in turn produced record efficiency for the respective cases. The results suggest under the ambient fabrication process, BSO nanorod-based CPSC achieved the highest PCE of ~13.4%, and on the other hand, the rhombohedral BTO nanorods claimed a massive ~15.02% PCE for the CPSC. Morphology modulation of BSO and BTO dictates the importance of structure-based performance analysis for CPSC. Employment of ZrO_2 spacer layer, NiO hole transport material (HTM) and graphitic carbon nanoparticle (CNP) counter electrode greatly influenced the results obtained. Moreover, BTO cubic nanoparticles, commercial TiO_2 paste and BSO nanoparticles were also investigated to compare the effect of nano-shape engineering.

2. Experimental section

2.1. Synthesis of BaSnO₃ nanorods

For the synthesis of $BaSnO_3$ following our earlier work, a homogeneous solution was prepared using 10 mM each of $BaCl_2 \cdot 2H_2O$ (Merck, UK) and $SnCl_4 \cdot 5H_2O$ (Alfa Aesar) thoroughly mixed under 30% H_2O_2 (Merck, UK) medium for 30 min [47]. By adding 25% NH_4OH (Merck, UK) solution to the mixture, the pH was maintained to 10. Then, dextran (M.W ca. 75 000, Alfa Aeasar) was added in a 1:6 wt ratio to control the growth. The resultant yellowish mixture was kept for 18 h for gel formation. Finally, the gel was preheated to 130 °C and calcined at 1000 °C for 8 h to produce the $BaSnO_3$. Synthesis of BSO spherical nanoparticles is given in supporting information.

2.2. Synthesis of Brookite TiO₂ nanorods

Following an earlier report, 5 g of titanium (IV) butoxide $(Ti(OBu)_4)$ and 5 g of isopropanol were mixed into 50 ml of DI water under magnetic stirring for 3 h [44]. The suspension was centrifuged and washed with DI water to collect the wet amorphous precipitate. It was then added to 50 ml solution of glycolic acid (1.05 M) under magnetic stirring for 2 h. As prepared, the suspension was transferred to an autoclave and heated to 90–100 °C for 20 h. After cooling to room temperature, and the pH was adjusted using concentrated NH_4OH to 12. Then, the sample was heated to 200 °C for 20 h using the autoclave. Finally, the product was cooled down to room temperature, washed, centrifuged and resuspended using DI water before drying at 60 °C for overnight. BTO nanostructure was redispersed in distilled water to prepare colloidal suspension for device fabrication. Synthesis of BTO cubic nanoparticles is given in supporting information.

2.3. Preparation of BaSnO₃ paste

1 g of perforated $BaSnO_3$ nanostructures and about 40 ml ethanol

were mixed with alternate magnetic stirring and ultrasonic treatment for a day. After that, 3.5 g terpineol, 3 g ethyl cellulose and 0.3 g acetylacetone were added into the white suspension and mixed with alternate magnetic stirring and ultrasonic treatment for a day. The resulting mixture was introduced into a rotary evaporator to remove excess ethanol. Finally, the paste was further treated with a ball mill.

2.4. Fabrication of device

The methodology was adopted from earlier reported articles with suitable modifications [48,49]. Fluorine doped tin oxide (FTO) glass substrate was etched in the first place, followed by standard cleaning procedures, which was common for both high-temperature and low-temperature carbon electrode-based devices. Next, titanium di-isopropoxide bis-(acetylacetonate) (TDBA) (75 wt% in isopropanol, Sigma-Aldrich) solution in 2-propanol (1:7 v/v) was prepared for deposition. The compact-TiO_2 layer was spin-coated at 2000 rpm for 30 s, then heated at 415 ± 10 °C for 30 min and cooled to room temperature. After that, BTO colloidal suspension in water was spin-coated 3 to 6 times at 2000 rpm for 30 s each case, followed by annealing at 100 °C for 5 min and further annealing on a hot plate at 180 °C for 1 h. Similarly, BSO paste diluted in ethanol 1:7 by weight was spin-coated at different spin coating speeds ranging from 3000 to 6000 for BSO based devices followed by annealing at 500 °C for 30 min in air. After cooling to room temperature, 0.1 M solution of Lithium (trifluoromethane sulfonyl) imide (LITFSI) in acetonitrile was spin-coated (3500 rpm for 20 s) on top of the c-TiO_2 layer followed by heating at 400 °C for half an hour. The ZrO_2 mesoporous layer was spin-coated with diluted ZrO_2 paste (Solarnix; v/v = 1:7 in ethanol) at 4000 rpm for 30 s and heated at 400 °C for 30 min (step 4). Next, the NiO layer was deposited using nano-oxide based paste (Solarnix, diluted at 1:7 v/v in ethanol) at 4000 rpm 30 s and sintered at 400 °C for 30 min. After cooling down to room temperature, the $CH_3NH_3PbI_3$ (MAPI) precursor solution with an appropriate amount (50 μl) was spin-coated at 1000 and 5000 rpm for 10 s and 20 s, respectively. During the last 10 s of rotation, chlorobenzene (400 μl) was splashed from the top and heated for 10 mins at 100 °C. Finally, the low-temperature carbon electrode was deposited by blade coating and heated at 100 °C for 10 min. The perovskite precursor solution was prepared by mixing MAI (163 gm) and PbI_2 (462 gm) in 3:7 DMSO (Dimethyl sulfoxide) :DMF (Dimethyl formamide) and heated for 1 h at 70 °C. The low-temperature carbon electrode was prepared according to our previously reported method with suitable modification. 2.5 g graphite and 2.5 g graphitic carbon nanoparticles were uniformly dispersed in 10.0 g terpineol via ball milling for 2 h. Then, 1.83 ml TTIP (Titanium tetraisopropoxide) and 0.2 ml Hac (glacial acetic acid) were added into the mixture by ball milling for another 10 h to gain homogenized carbon paste.

2.5. Characterization techniques

X-ray diffraction (XRD) was performed on an X'pert pro MPD XRD of PANanalytical with Cu Kα1 radiation (λ = 1.5406 Å). Raman spectroscopy was carried out using Renishaw Reflex micro-Raman spectrometer with an argon ion, 514 nm laser. A Tecnai G2 30ST (FEI) high-resolution transmission electron microscope (TEM) operating at 300 kV was used for transmission electron microscopy (TEM) of CNPs. The cross-sectional layer thickness measurement and elemental mapping of the PSC were recorded on a scanning electron microscope (SEM-EDX), (LEO 430i, Carl Zeiss). XRD study of the fabricated devices was executed on an X'pert pro MPD XRD of PAN analytical with Cu Kα radiation (λ = 1.5406 Å). The charge-transport properties of different ETLs on perovskite were measured by photoluminescence spectroscopy (PL: FLS1000 Photoluminescence Spectrometer, Edinburgh instruments). Further, photovoltaic measurements of the PSC were executed under 1000 W/m² of light illumination from a Wacom AAA continuous solar simulator (model type: WXS-210S-20, AM1.5G) and an EKO MP-160i *I-V* Tracer.

EIS assessment was performed with an AUTOLAB frequency analyzer setup equipped with an AUTOLAB PGSTAT 10, and a Frequency Response Analyzer (FRA) module under the dark condition having a frequency range from 1 MHz to 0.1 Hz at the 0.80 V open-circuit voltage. The Z-view software (version 3.4d, Scribner Associates, Inc., USA) was used to fit the experimental data. Incident photon to current efficiency (IPCE) measurement was carried out on a BENTHAM PVE300 Photovoltaic EQE (external quantum efficiency) and IQE (internal quantum efficiency) solution under 350–750 nm wavelength using a tungsten halogen lamp source.

3. Results and discussion

Analysis of morphological and optical properties of BSO and BTO nanostructures.

In order to understand the formation of BSO and BTO nanostructures along with their morphology, various characterization techniques were utilized, namely XRD, Raman, FESEM and HRTEM. The crystallinity and phase purity of as prepared BSO nanostructures from two different methods were first scrutinized with XRD. The pure phase of BSO according to the JCPDS (joint committee on powder diffraction standards) card no. 74–1300 is reported to be a cubic phase perovskite having lattice parameter a = 4.108 nm. The formation of pure phase BSO was confirmed without having any SnO_2 phase, as shown in Fig. 1a, and the Reitveld analysis suggests a lattice parameter of a = 4.105 ± 0.004 nm for the $BaSnO_3$ perovskite phase.

It is crucial to recognize different bond vibrations in the BSO lattice using Raman scattering measurement represented in Fig. 1b. According to group theory a perfect $Pm\overline{3}m$ perovskite structure should have three IR active modes with F_{1u} symmetry without Raman active modes, the spectra of the M−point optical phonons in BSO have been studied using Raman scattering. The transverse (TO) and longitudinal (LO) optical phonon modes near 131, 248, and 412 cm^{-1} are accountable for LO_1, TO_2, and LO_2. On the other hand, the $TO_1 + LO_2$, LO_3, and $2LO_2$ phonon modes with high-frequency overtones are allocated at 552, 723, and 832 cm^{-1}, respectively [50].

To interpret the surface, size, and morphology of different types of BSO nanostructures, SEM and TEM investigations were performed. The SEM results dictate two different microstructural surfaces achieved from two different synthesis methods. Fig. 2a and S1a (supporting information, SI) indicate the formation of rod and spherical particles of BSO, respectively. Using the TEM bright-field image the average diameter of the nanorods was found to be ∼ 50 nm, whereas the spherical particles had an average diameter of ∼ 38 nm. In Fig. 2b and S1b, the TEM bright-field images are shown for the synthesized BSOs having different shapes at different magnifications. Further, the interlayer spacing of the most intense (1 1 0) peak as 0.291 nm is shown in the HR-TEM images given in Fig. 2c and S1c. A clear signature of the polycrystalline nature of BSO can be understood from the selected area electron diffraction (SAED)

patterns with the formation of crystalline planes (1 1 1), (1 1 0), and (2 0 0) as shown in Fig. 2d and S1d.

Similar to the BSO samples, the BTO nanostructures were characterized with XRD and Raman spectra to determine the phase purity. In Fig. 3a the peaks near 25.34°, 31.5°, 36.2°, 40°, 47.5° and 55.5° due to the (1 2 0), (1 1 1), (1 2 1), (0 1 2), (0 2 2), (2 3 1) and (2 4 4) planes are the major characteristics planes for BTO. However, XRD is not enough to prove the formation of single-phase BTO due to the possibility of overlapping of anatase (1 0 1) at 25.28° and (1 2 0) reflection of brookite at 25.34°. But it is confirmed that diffraction peaks of rutile, TiO_2(B) or other titanium oxide compounds are absent in the XRD pattern. Ruling out the existence of anatase impurities can be done via Raman spectra. Fig. 3b shows that all 16 Raman peaks match the literature in the range of 100 cm^{-1} to 700 cm^{-1}. The Raman bands for A_{1g} (127, 152, 195, 247, 413, and 637 cm^{-1}), B_{1g} (214, 322 and 500 cm^{-1}), B_{2g} (367, 394, 462 and 585 cm^{-1}), and B_{3g} (170, 286 and 545 cm^{-1}) of BTO clarifies inexistence of anatase (characteristics peak at 518 cm^{-1}), rutile (characteristics peak at 442 cm^{-1}) or other impurities. The XRD and Raman characterizations as a whole imply pure phase BTOs.

Analysis of the 3D (three dimensional) surfaces of the BTO synthesized from two different methods was done using the SEM, which resembles rod-shaped nanostructures in Fig. 4a and pseudo-cubes in Fig. S2a (SI). TEM and HR-TEM characterizations of BTO reveal the 2D (two dimensional) morphological projection and particle sizes of synthesized BTOs, as shown in Fig. 4b-c and S2b-c (SI). The synthesized rod-shaped BTOs have diameters in the range of 28 to 45 nm, and the cube-like (square in 2D) nanostructures have 35 to 80 nm particle size. The crystallinity and polycrystalline character of the BTOs are well confirmed from the HR-TEM images and the SAED pattern, as shown in Fig. S4 and S2 (SI).

Nitrogen physisorption measurements of all the samples were measured using a Quantachrome (iQ3) instrument after evacuation at 150 °C for 4 h. The specific surface area was calculated by the Brunauer-Emmett-Teller (BET) method. Fig. S3, SI indicates the comparative analysis of BET surface area of the alternating ETL samples. The surface area values are found in order of BSO particle < BTO cube < BSO rod < BTO rod within 18–30 m^2/g. It has been clearly observed from the TEM morphologies belonging to both BSO and BTO that they excel in visible porosity and reflect better surface area compared to other traditional oxides. The stacked-plane pore geometry throughout plate-like microstructural framework for BTO and perforated nanostructures for BSO was reasonably visible in TEM, evidencing type IV isotherm and type H3 hysteresis caused by tensile strength effect during gas condensation process and thus formed a higher order of pore tensile strength which is common, especially for the oxide-based nanostructures [51]. However, the specific surface area values of all the samples were not the only factor contributing to the electrical characteristics of the corresponding device. Although, the morphological distribution excels a noticeable impact on the PV performance. As observed in Table 1, BTO rods exhibit
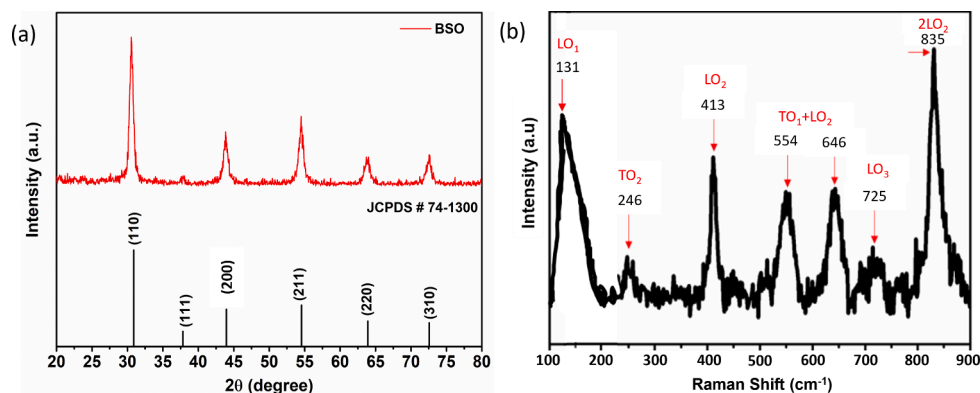

Fig. 1. Structural and optical properties of BSO. (a) X-ray diffraction pattern; (b) Raman spectrum.
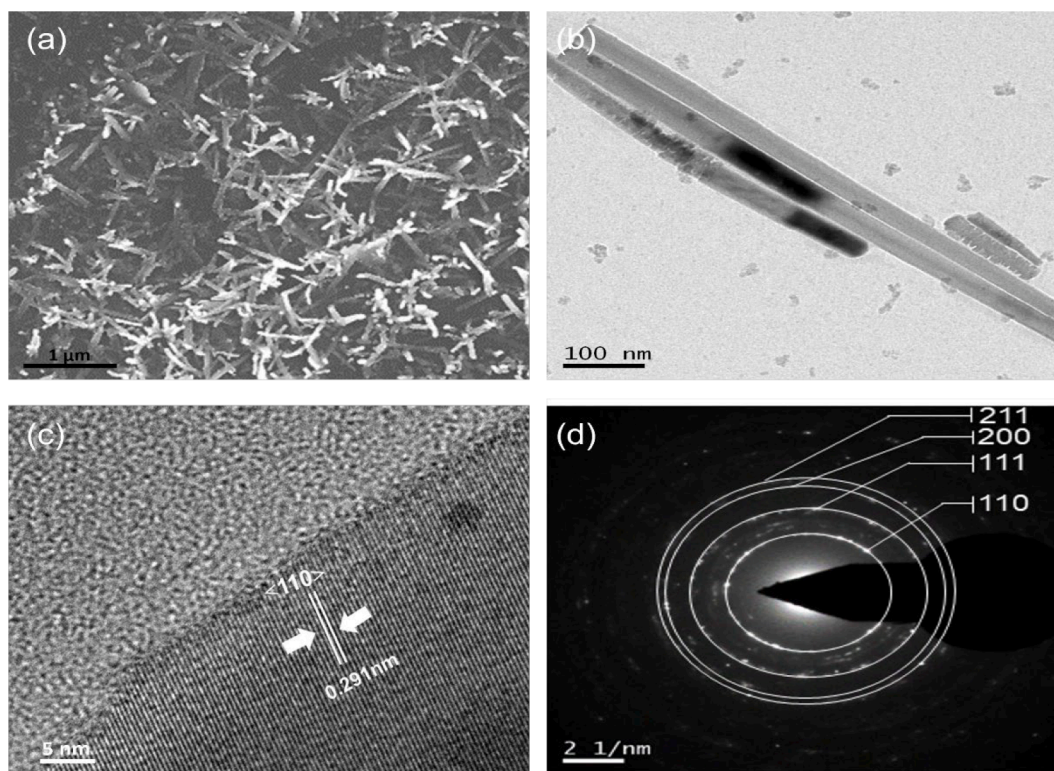
Fig. 2. Microscopic characterizations of BSO nanorods. (a) SEM microstructural image, (b) TEM bright-field image, (d) HRTEM image, and (e) SAED pattern of the synthesized BSO nanorods, respectively.
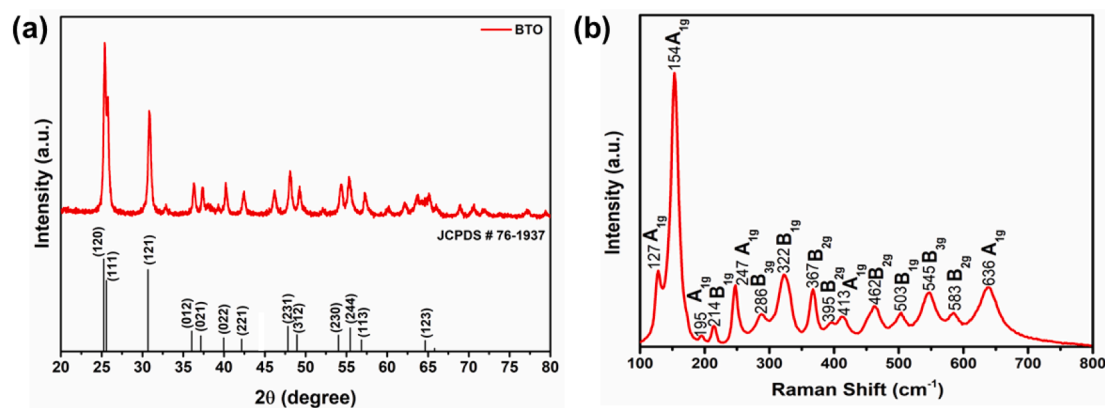

Fig. 3. Structural and optical properties of BTO. (a) X-ray diffraction pattern; (b) Raman spectrum.

higher efficiency than BTO rods due to their one-dimensional (1D) shape, generating more facets for the excited electrons. On the other hand, nanorods mostly dominate over corresponding particle structures due to their anisotropic orientation that diminishes internal grain boundaries and electron trapped states, further facilitating the excited electrons to flow in a specific direction which minimizes electron recombination. Therefore, a combined synergistic factor of morphology distribution with dimension and the surface area should enable an enhanced electron diffusion over PV performance [52].

3.1. Structural and photovoltaic analysis of devices

The structure of fabricated devices is shown in Fig. 5a, along with generalized cross-sectional SEM of BTO and BSO layered CPSCs. Among the different spin coating speeds utilized for BSO structured cells, the best performance was obtained at 4000 rpm. On the other hand, the BTO

layer with four-round of spin coating achieved maximum efficiency. Then again, before going into the performance of the devices, the photoluminescence of various ETL and perovskite contact was examined to realize the nature of charge transfer, as shown in Fig. 5b. All the samples showed a strong band-edge emission peak near 770 nm when excited at a wavelength of 473 nm. Usually, the most intense emission peak should be observed for glass/MAPbI$_3$ film, whereas the inclusion of ETL will exhibit a quenching effect. After excitation of electrons in MAPbI$_3$, they will fall back to the ground state with the release of energy in three different ways, namely radiative transition (it contains photoluminescence), non-radiative transition (likely to have an inter-system crossing or internal conversion), and energy transfer and quenching [53]. Due to the quenching effect, the excited electrons of the films will come back to the ground state by energy transfer to the mesoporous ETLs, which act as the quenching layer. Without the quenching layer, the energy is released by photoluminescence mainly, which produces
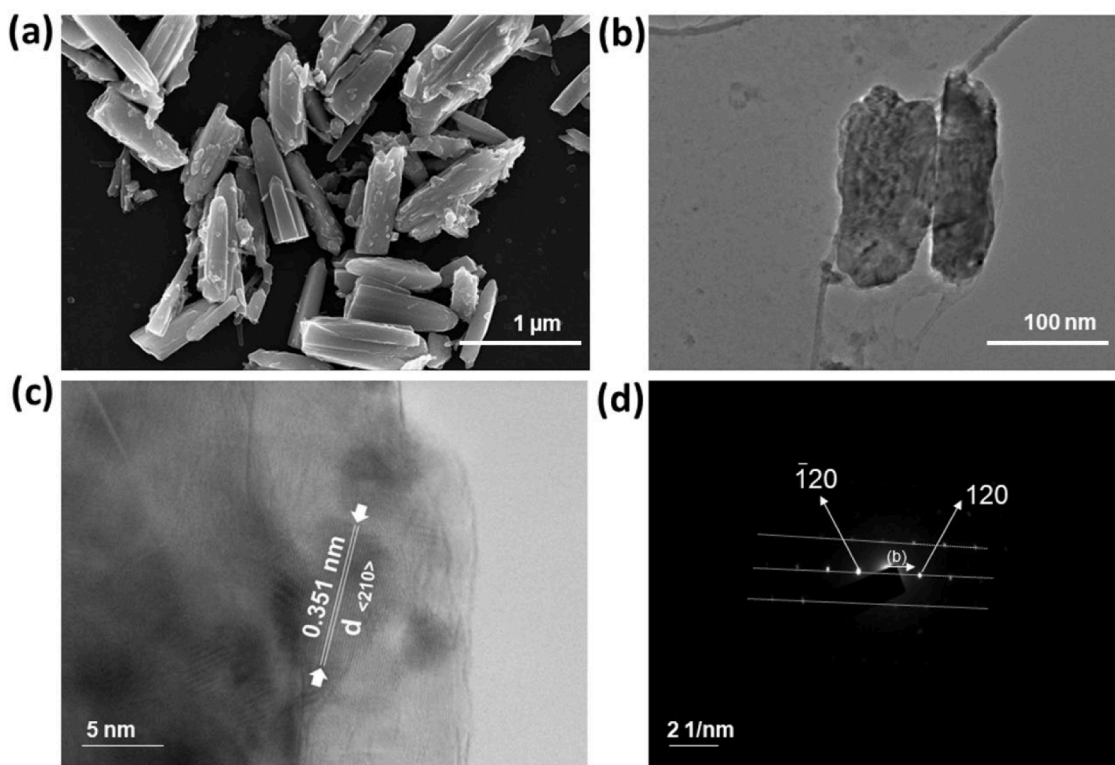
Fig. 4. Microscopic characterizations of BTO nanorods. (a) SEM image of the BTO nanorods; (b) TEM bright-field image; (c) HRTEM image; (d) SAED pattern indicating major crystalline planes.

Table 1
Photovoltaics performance of devices at 1 Sun AM 1.5 having an active area of 0.16 cm^2 (average is given based on 10 devices for each case with statistical error).

Device type		Jsc (mA/cm^2)	Voc (mV)	Fill factor (FF) %	PCE (%)	Rs (Ω)	Rct (Ω)	Rrec (Ω)
BSO rod	Average	20 ± 1.2	960 ± 35	60 ± 1	12.1 ± 1.1	65 ± 7	75 ± 7	145 ± 6
	Champion	21.7	1004	61.5	13.4	55.54	67.51	138.7
BSO particles	Average	19.3 ± 1.8	938 ± 45	57.8 ± 1.5	11.4 ± 1	70 ± 9	90 ± 6	160 ± 10
	Champion	21.25	989.2	59.5	12.50	61.8	82.12	144.6
BTO rod	Average	20.6 ± 1.4	1020 ± 38	62.6 ± 1.4	13.6 ± 1.2	52 ± 5	55 ± 7	736 ± 18
	Champion	22.1	1062.5	64	15.02	46.1	46.8	719.5
BTO cube	Average	20.2 ± 1	1010 ± 30	61.5 ± 0.8	12 ± 1.8	55 ± 7	105 ± 15	740 ± 15
	Champion	21.42	1047.0	62.5	14.0	47.6	94.2	714.6
Commercial TiO$_2$	Average	19.7 ± 1.4	995 ± 30	60 ± 1.1	11.6 ± 1.5	60 ± 6	205 ± 20	475 ± 40
	Champion	21.14	1026.25	61.2	13.27	51.4	180	450.2

the sharpest emission peak of the glass/MAPbI$_3$ film. However, the presence of the ETL layer will force the energy of excited electrons to be released by energy transfer and quenching which can be judgmental for the quenching layers' charge transfer efficiency. In Fig. 5b, the nanorod structured BTO as ETL showed the most suitable quenching effect with the frailest emission peak near 770 nm, which suggests a large part of electronic energy is released by energy transfer. Although, according to previous studies, it does not confirm the best output photovoltaic performance of devices due to other photoelectrical properties of an entire CPSC [45,53]. Also, a generalized electron transfer process for BSO and BTO based devices is given in Fig. 5c for better understanding [38,40]. For further investigation of the quenching effect and electron diffusion, the time-resolved PL decay measurement was carried out at a peak emission of ~ 770 nm (Fig. 5d). The PL decay of the neat MAPbI$_3$ film exhibits a time-constant of $\tau_e = 75 \pm 10$ ns. The addition of the different electron quenching layers accelerates the PL decay, and the observed time constants are given in Table T3, SI. The best scenario was observed for the BTO nanorod ETL achieving $\tau_e = 3.5 \pm 0.5$ ns and the least favoural observation was for the BSO particle having $\tau_e = 11.2 \pm 0.6$. The PL decay dynamics were modeled by calculating the number and

distribution of excitations in the film n(x,t) according to the one-dimensional diffusion equation.

$$\frac{dn(x,t)}{dt} = D\frac{\left(d^2 n(x,t)\right)}{dx^2} - k(t)n(x,t) \tag{1}$$

where D is the diffusion coefficient, and k(t) is the PL decay rate in the absence of any quencher material [54]. Following previous research, the average diffusion length L_D of the species was then determined from $L_D = \sqrt{D\tau}$, where τ is the recombination lifetime in the absence of a quencher. The diffusion coefficients for electrons were estimated depending on the quenching layer, and the results from the diffusion model fits are shown in Fig. 5d, and the parameters are summarized in Table T3, SI. The observed diffusion length for the BTO nanorod is ~ 500 nm, whereas, for BSO particle, it has has the least diffusion length of ~ 400 nm. The diffusion lengths closely resemble the recombination effect in the devices as high diffusion length is indicative of lesser recombination rates enhancing the collection probability [55,56]. The raw data related to the modelled fit shown in Fig. 5d is displayed in the supporting information file (Fig. S5).

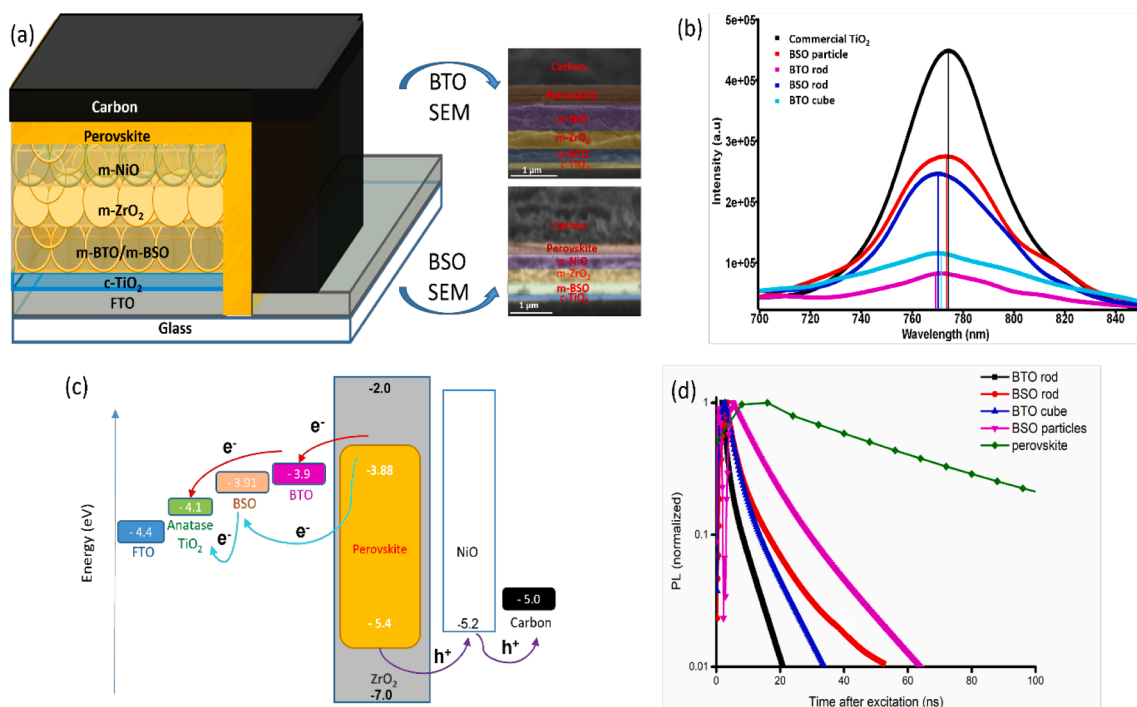Investigation of photovoltaics performances of various

Fig. 5. (a) Generalized structural representation of the fabricated CPSC devices along with cross-sectional SEM of the BTO and BSO based champion devices; (b) Steady-state photoluminescence (PL) spectra of glass/mp-X/MAPbI$_3$ (X = BSO rod, BSO particle, BTO rod, BTO cubic particle, commercial TiO$_2$) films with an excitation wavelength of 473 nm; (c) Diagram of energy levels (relative to the vacuum) of the different functional layers in the devices; (d) Time-resolved PL measurements taken at the peak emission wavelength of the triiodide perovskite with different electron quencher layer along with stretched exponential fits to the blank halide perovskite and fits the quenching samples by using the diffusion model described in the text.
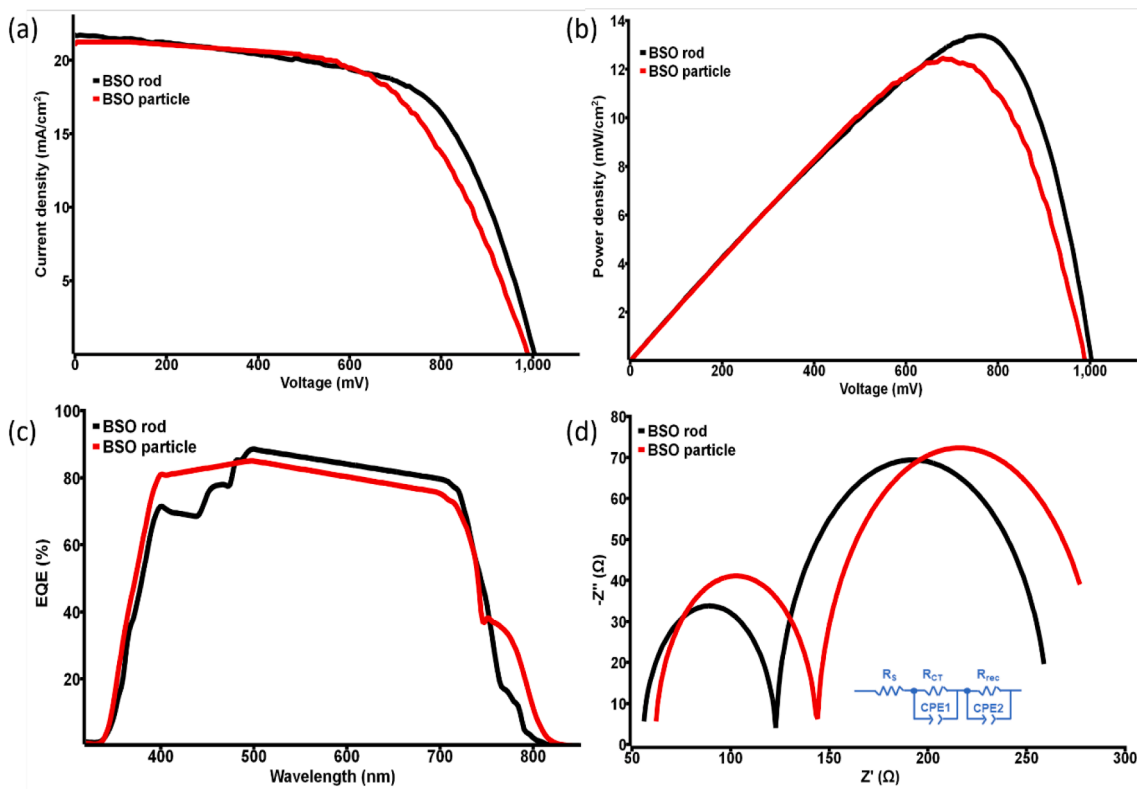

Fig. 6. Photovoltaic performance of champion BSO devices. (a) Current density vs. voltage plot; (b) Power density vs. voltage plot; (c) EQE of the champion devices; (d) EIS representation along with the fitted electrical circuit diagrams.

nanostructured BSO and BTO as ETL was carried out with a batch of 10 devices in each case. The BSO based devices had two categories, one with rod-shaped BSO ETL, and the other was spherical particle type BSO. For both types of BSO devices, the spin coating rpm (rotation per minute) was varied from 3000 to 6000 rpm. The observed trend suggests that the 4000 rpm spin coating is the most efficient for both BSO devices, as shown in Table T1, SI. Among the rod and particle nanostructures, the rod-shaped BSO achieved a maximum PCE of 13.4% along with Jsc, Voc and FF of 21.7 mA/cm^2, 1004 mV and 61.5%, respectively. On another side, the particle type BSO was able to produce a maximum PCE of 12.5%, having Jsc, Voc and FF of 21.25 mA/cm^2, 989.2 mV and 59.5%, respectively. Fig. 6a and 6b demonstrate the nature of the *J-V* (current density–voltage) and *P-V* (power density–voltage) curves, respectively, for the champion devices configured with BSO nanostructures. The devices with high Jsc indicate a high collection probability of carriers generated by light absorption. The observation suggests the collection probability of BSO rod devices is much higher than that of particles as the predecessor has ∼ 1.05 times higher current density. Next, the hysteresis effect was investigated for the devices. *J-V* hysteresis occurs in perovskite devices while voltage scanning in forward and reverse biased conditions. The main reason behind hysteresis is the large capacitive effect of halide perovskite. In this report, the hysteresis behaviour of champion devices has been shown in Fig. S4 a and b, SI for the BSO-CPSC. The low hysteresis behaviour indicates a decrease in interface trap densities, enhanced charge diffusion lengths and low surface recombination [33,57]. Concerning the PCE, the external quantum efficiency (EQE) and EIS (electrochemical impedance spectroscopy) were analyzed for the BSO devices. Both the champion BSO rod and particle-based devices obtained the highest EQE of ∼ 90%, and the integrated photocurrent density calculated from that was 19.2 mA/cm^2 and 19.02 mA/cm^2, respectively (Fig. 6c). The effect of optical losses caused by transmission and reflection produces slightly reduced values of integrated photocurrent densities from the original values achieved via *J-V* characterization.

EIS is a valuable technique to understand the outcome of photovoltaic parameters like the Jsc, Voc and FF. The series resistance Rs corresponds to the resistance of FTO coated glass and the cell's contact resistance. The Rs for the champion BSO rod device is lower than that of the champion device with BSO particles, implying BSO rod devices should produce better FF. As shown in Fig. 6d (circuit diagram inset), the nature of the EIS plot explains that the charge transfer resistance (Rct) of BSO rod PSC is slightly lower than the spherical particle-based PSC. Usually, a lower Rct value indicates better charge collection ability between the counter electrode and perovskite, which favourably increases the photocurrent density of the device. Due to the small difference between the Rct values of both types of BSO devices, the obtained Jsc values are pretty close. On the other hand, the charge recombination resistance (Rrec), which reflects the recombination process at the interface between the perovskite and BSO, is higher in the case of the BSO rod device. Smaller charge recombination resistance means the interfacial recombination is more pronounced for a particular device. The devices with BSO particles suffer from a higher rate of interfacial charge recombination, reducing the overall PCE of the devices. The particle size and shape hugely affected the device performance, which is also related to the grain boundary of the nanomaterials [15,58]. The PL spectra in Fig. 5b shows a blue shift of PL peak for the BSO rod compared to BSO particles (771 nm to 767 nm) which proves the lowering of trap states of the perovskite film growth in contact with the BSO rod revealing an efficient reduction of non-radiative recombination centres. Thus, the rod structured BSO is expected to improve the electron diffusion length in photoanode film remarkably by allowing a direct conduction route for electron transport due to lesser grain boundary traps which are reflected in the outcome of photovoltaic performances [59].

The observed trend of the photovoltaic performances of the BTO based devices was fascinating. The varying number of BTO deposition in

3 to 6 steps suggests the BTO layer's suitable thickness indicating the highest PCE for four-step deposition. A detailed photovoltaic result related to the number of spin coating steps is mentioned in Table T2, SI. During the comparative study of the two BTO structures, the *J-V* characterization showed the highest PCE for BTO rod-structured devices, although the cubic BTO devices are not far behind. The performance of BTO devices was also compared with the devices prepared from commercial TiO$_2$ paste. All the TiO$_2$ based devices were able to achieve Voc of>1000 mV, as shown in Fig. 7a, and among them, CPSC with BTO rod ETL attained the maximum Voc of 1062.5 mV along with Jsc of 22.1 mA/cm^2 and FF of 64%. Similarly, the champion device with BTO nanocubes showed a high Voc of 1047 mV, Jsc of 21.42 mA/cm^2 and FF of 62.5%. The commercial TiO$_2$ paste with ∼ 13.3% maximum efficiency was the least efficient compared to two different types of BTO devices, which can be seen from the detailed values given in Table 1. Usually, a solar cell with a higher voltage has a larger possible FF since the "rounded" portion of the IV curve takes up less area. The study exemplifies similar behaviour. The champion BTO rod-based device achieved a fill factor > 2.4% to that of the cube-based device. The hysteresis behaviour of champion BTO devices is given in Fig. S4c and d, SI, which explains the better performance of BTO nanorod devices compared to nanocubes. To confirm the Jsc values obtained from the measurement using solar simulator, EQE (external quantum efficiency) was analyzed for the CPSCs with the BTO layer. The integrated Jsc calculated from the IPCE spectrum matches closely with the measured values, as shown in Fig. 7c. Strong IPCE coverage in the range of ∼ 500 to 780 nm for BTO based devices expresses significant improvement in interface quality and efficient charge carrier transport compared to commercial TiO$_2$ based ETL. Furthermore, EIS was performed to realize the electrical properties of interfaces on the basis of carrier recombination, charge transfer and the inner series resistance within the variety of TiO$_2$ based devices. The lower Rs and Rct values of BTO and commercial TiO$_2$ devices effectively make them strong candidates for high Jsc and fill factor, although the deciding factor here was the recombination resistance denoted by Rrec. The low rate of charge recombination is regulated by the high Rrec value, which actually causes an upper-hand for BTO as ETL instead of commercial TiO$_2$, as shown in Fig. 7d. However, BTO nanorods and BTO nanocubes also manifested contrasting photovoltaic performances, with BTO nanorods having the edge over the cubic counterpart. According to an earlier report, the large surface area of nanoparticles utilized as ETL can enhance the cohesion of the ETL/perovskite contact, lowering the number of surface defect traps and refining the morphology of perovskite [40,60]. Better IPCE coverage in the region of ~500 to 780 nm for BTO rod-based devices confirms improved perovskite film and interface quality with the contact of the transport layer proving the surface defect reduction [38,53]. On the other side, a significant shift of wavelength was observed for the BTO rod towards the blue region (Fig. 5b) in the PL spectra, which evidences the passivation of deep level traps at grain boundaries reducing the recombination centres influencing higher charge transfer for perovskite film [61]. Similarly, reduced surface defects due to the diminished grain boundary of nanorods are expected to play a key role in enhancing the electrical property of devices. The performance variation of the BSO and BTO as ETL is very significant at this point. The PL plots given in Fig. 5b and d showed excellent charge transfer efficiency of the BTO nanostructures compared to BSO due to the quenching effect as mentioned earlier; the significant point in the performance output of devices was the charge transfer, charge recombination and inner resistances obtained from EIS. Usually, a small parabola in the high-frequency region of the EIS spectra suggests a lower Rct value indicating a high charge transfer rate between the transport layer and perovskite. This, in turn, gives higher values of FF and Jsc, which is evident from our observations for the BTO devices, as mentioned in Table 1. On the other hand, a large parabola with a high value of Rrec is always excellent for a device as it explains a lower rate of charge recombination, increasing the Voc of the device. These EIS data indicate the reason behind higher Jsc of BTO rod compared to BSO rod,
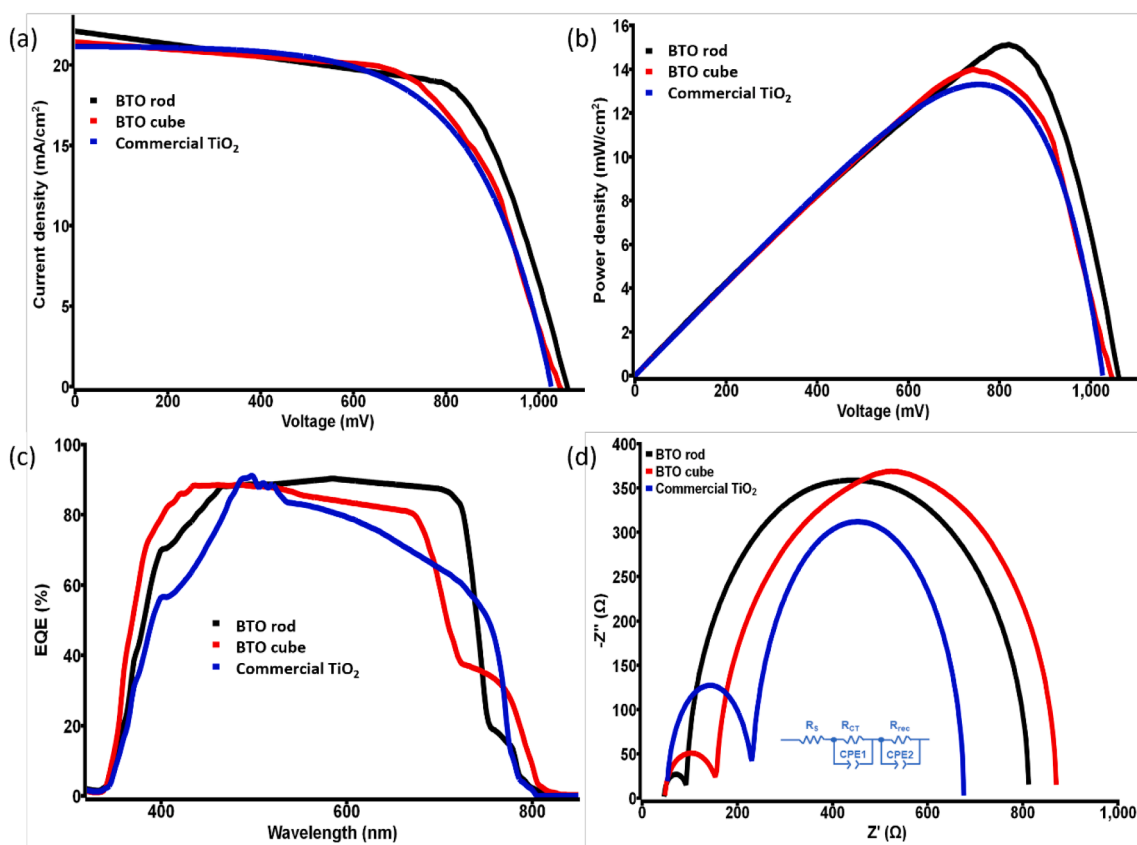
Fig. 7. Photovoltaic performance of champion BTO and commercial TiO$_2$ based devices. (a) Current density vs. voltage plot; (b) Power density vs. voltage plot; (c) EQE of the champion devices; (d) EIS representation along with the fitted electrical circuit diagrams.

higher value of Jsc for BSO rod compared to BTO cubes and higher values of Jsc for both the BSO nanostructures concerning commercial TiO$_2$ in the CPSC devices. Finally, the stability study of the unencapsulated cells was carried out, as shown in Fig. S6, which indicates BSO structured CPSCs are more stable in ambient conditions compared to the TiO$_2$ based ones. Irrespective of the nanostructures, both types of devices showed excellent stability under ambient conditions, near 1000 hrs, with a loss of ~20 of initial efficiency when stored in the dark. Some studies reported earlier on the strong electron extraction ability of TiO$_2$ from iodide (I⁻) as electrodes in DSSC (dye-sensitized solar cell) and from organic materials as photocatalysts [62]. That is why researchers considered the extraction of electrons from I⁻ by TiO$_2$ and oxidizing I⁻ to iodine in the presence of light as a deforming factor of the perovskite crystal structure; as a result, little low stability was observed for BTO based devices [63,64]. Stabilized PCE at maximum power point was observed for all devices, and results are summarized in Fig S6c. The devices took ~36 ± 10 s to achieve stabilized PCE at maximum power points. As devices were non-encapsulated, continuous light soaking (Solar simulator 1 Sun, AM 1.5) focused on the device creates heating in the CPSC and significantly increases cell temperature. The increase in device temperature while the surrounding environment is at room temperature produces thermal stress in the system. This thermal stress is the reason behind poor light-soaking stability [17,18,63,65]. The long stability of CPSC in ambient conditions is always a hot topic of research; however, this work aims to talk about the structural effect of different nanomaterials as ETL, and we believe this can provide further advancement in the field of perovskite devices.

4. Conclusion

In conclusion, different BSO and BTO nanostructures have been

successfully synthesized and employed as ETL for CPSC. The morphology variation of BSO and BTO active layers greatly altered the electron conduction, and the rod-shaped nanostructures of both BSO and BTO came on top resulting in 13.4% and 15.02% of PCE, respectively in ambient fabrication conditions. It dictates the importance of grain boundary trap passivation via structural modulation of nanomaterials, which can hugely improve the performances of devices. Furthermore, we have investigated the suitable fabrication engineering of the nanostructured ETL for these CPSCs. The PL measurement and EIS analysis have been considered as essential tools to recognize the effect of morphological tuning of electron transport materials for the devices. This report indicates the excessive charge recombination rate as the reason behind the slightly diminished performances of BSO based CPSCs. At the same time, our experimentation significantly indicates the importance of various nanostructures of the same material for the application in perovskite solar cells. We believe our findings could pave the way to future developments in the area of CPCSs using structurally tuned nanomaterials and low-cost fabrication techniques for their practical implementation.

CRediT authorship contribution statement

Shubhranshu Bhandari: Conceptualization, Methodology, Formal analysis, Investigation, Writing – original draft, Visualization. **Anurag Roy:** Investigation, Writing – review & editing, Visualization. **Tapas Kumar Mallick:** Conceptualization, Investigation, Writing – review & editing, Visualization, Supervision, Project administration, Funding acquisition. **Senthilarasu Sundaram:** Conceptualization, Investigation, Writing – review & editing, Visualization, Supervision, Project administration, Funding acquisition.

Declaration of Competing Interest

The authors declare that they have no known competing financial interests or personal relationships that could have appeared to influence the work reported in this paper.

Acknowledgement

Appendix A. Supplementary data

Supplementary data to this article can be found online at https://doi.org/10.1016/j.cej.2022.137378.

References

[1] E.H. Jung, N.J. Jeon, E.Y. Park, C.S. Moon, T.J. Shin, T.-Y. Yang, J.H. Noh, J. Seo, Efficient, stable and scalable perovskite solar cells using poly(3-hexylthiophene), Nature 567 (7749) (2019) 511–515.

[2] A. Kojima, K. Teshima, Y. Shirai, T. Miyasaka, Organometal halide perovskites as visible-light sensitizers for photovoltaic cells, J. Am. Chem. Soc. 131 (2009) 6050–6051, https://doi.org/10.1021/ja809598r.

[3] H.-S. Kim, C.-R. Lee, J.-H. Im, K.-B. Lee, T. Moehl, A. Marchioro, S.-J. Moon, R. Humphry-Baker, J.-H. Yum, J.E. Moser, M. Grätzel, N.-G. Park, Lead iodide perovskite sensitized all-solid-state submicron thin film mesoscopic solar cell with efficiency exceeding 9%, Sci. Rep. 2 (1) (2012) https://doi.org/10.1038/srep00591.

[4] A. Mei, X. Li, L. Liu, Z. Ku, T. Liu, Y. Rong, et al., A hole-conductor{ extendash}free, fully printable mesoscopic perovskite solar cell with high stability, Science (80-) 345 (2014) 295–298, https://doi.org/10.1126/science.1254763.

[5] <https://www.nrel.gov/pv/cell-efficiency.html> (2022). Best Research-Cell Efficiency Chart n.d.

[6] M. Khalid, A. Roy, S. Bhandari, P. Selvaraj, S. Sundaram, T.K. Mallick, Opportunities of copper addition in CH3NH3PbI3 perovskite and their photovoltaic performance evaluation, J. Alloy. Compd. 895 (2022), 162626, https://doi.org/10.1016/j.jallcom.2021.162626.

[7] G. Grancini, C. Roldán-Carmona, I. Zimmermann, E. Mosconi, X. Lee, D. Martineau, S. Narbey, F. Oswald, F. De Angelis, M. Graetzel, M.K. Nazeeruddin, One-Year stable perovskite solar cells by 2D/3D interface engineering, Nat. Commun. 8 (1) (2017), https://doi.org/10.1038/ncomms15684.

[8] D. Forgacs, K. Wojciechowski, O. Malinkiewicz, Perovskite Photovoltaics: From Laboratory to Industry BT - High-Efficient Low-Cost Photovoltaics: Recent Developments. In: Petrova-Koch V, Hezel R, Goetzberger A, editors., Cham: Springer International Publishing; 2020, p. 219–55. doi: 10.1007/978-3-030-22864-4_10.

[9] N. Torabi, A. Behjat, Y. Zhou, P. Docampo, R.J. Stoddard, H.W. Hillhouse, et al., Progress and challenges in perovskite photovoltaics from single- to multi-junction cells, Mater. Today Energy 12 (2019) 70–94, https://doi.org/10.1016/j.mtener.2018.12.009.

[10] R. Wang, M. Mujahid, Y. Duan, Z.-K. Wang, J. Xue, Y. Yang, A review of perovskites solar cell stability, Adv. Funct. Mater. 29 (2019) 1808843, https://doi.org/10.1002/adfm.201808843.

[11] A. Abate, J.-P. Correa-Baena, M. Saliba, M.S. Su'ait, F. Bella, Perovskite solar cells: from the laboratory to the assembly line, Chem. Eur. J. 24 (13) (2018) 3083–3100.

[12] H.-S. Kim, J.-Y. Seo, N.-G. Park, Material and device stability in perovskite solar cells, ChemSusChem 9 (2016) 2528–2540, https://doi.org/10.1002/cssc.201600915.

[13] A. Roy, A. Ghosh, S. Bhandari, S. Sundaram, T.K. Mallick, Perovskite solar cells for BIPV application: a review, Build 10 (7) (2020) 129.

[14] N. Aristidou, I. Sanchez-Molina, T. Chotchuangchutchaval, M. Brown, L. Martinez, T. Rath, S.A. Haque, The role of oxygen in the degradation of methylammonium lead trihalide perovskite photoactive layers, Angew. Chem. Int. Ed. 54 (28) (2015) 8208–8212.

[15] N.-G. Park, Research direction toward scalable, stable, and high efficiency perovskite solar cells, Adv. Energy Mater. 10 (2020) 1903106, https://doi.org/10.1002/aenm.201903106.

[16] F. Meng, A. Liu, L. Gao, J. Cao, Y. Yan, N. Wang, M. Fan, G. Wei, T. Ma, Current progress in interfacial engineering of carbon-based perovskite solar cells, J. Mater. Chem. A 7 (15) (2019) 8690–8699.

[17] L. Cojocaru, S. Uchida, Y. Sanehira, V. Gonzalez-Pedro, J. Bisquert, J. Nakazaki, T. Kubo, H. Segawa, Temperature effects on the photovoltaic performance of planar structure perovskite solar cells, Chem. Lett. 44 (11) (2015) 1557–1559.

[18] S. Bhandari, A. Roy, A. Ghosh, T.K. Mallick, S. Sundaram, Perceiving the temperature coefficients of carbon-based perovskite solar cells, Sustain Energy Fuels 4 (2020) 6283–6298, https://doi.org/10.1039/D0SE00782J.

[19] S.-W. Lee, S. Kim, S. Bae, K. Cho, T. Chung, L.E. Mundt, S. Lee, S. Park, H. Park, M. C. Schubert, S.W. Glunz, Y. Ko, Y. Jun, Y. Kang, H.-S. Lee, D. Kim, UV degradation and recovery of perovskite solar cells, Sci. Rep. 6 (1) (2016), https://doi.org/10.1038/srep38150.

[20] Y. Rong, L. Liu, A. Mei, X. Li, H. Han, Beyond efficiency: the challenge of stability in mesoscopic perovskite solar cells, Adv. Energy Mater. 5 (2015) 1501066, https://doi.org/10.1002/aenm.201501066.

[21] M. Hadadian, J.-H. Smått, J.-P. Correa-Baena, The role of carbon-based materials in enhancing the stability of perovskite solar cells, Energy Environ. Sci. 13 (2020) 1377–1407, https://doi.org/10.1039/C9EE04030G.

[22] H. Chen, S. Yang, Carbon-based perovskite solar cells without hole transport materials: the front runner to the market? Adv. Mater. 29 (2017) 1603994, https://doi.org/10.1002/adma.201603994.

[23] M.A. Deshmukh, S.-J. Park, B.S. Hedau, T.-J. Ha, Recent progress in solar cells based on carbon nanomaterials, Sol. Energy 220 (2021) 953–990, https://doi.org/10.1016/j.solener.2021.04.001.

[24] S. Bhandari, A. Roy, M.S. Ali, T.K. Mallick, S. Sundaram, Cotton soot derived carbon nanoparticles for NiO supported processing temperature tuned ambient perovskite solar cells, Sci. Rep. 11 (2021) 23388, https://doi.org/10.1038/s41598-021-02796-w.

[25] M.K.A. Mohammed, High-performance hole conductor-free perovskite solar cell using a carbon nanotube counter electrode, RSC Adv. 10 (2020) 35831–35839, https://doi.org/10.1039/D0RA05975G.

[26] P. Calado, A.M. Telford, D. Bryant, X. Li, J. Nelson, B.C. O'Regan, et al., Evidence for ion migration in hybrid perovskite solar cells with minimal hysteresis, Nat. Commun. 7 (2016) 13831, https://doi.org/10.1038/ncomms13831.

[27] I. Levine, P.K. Nayak, J.-W. Wang, N. Sakai, S. Van Reenen, T.M. Brenner, S. Mukhopadhyay, H.J. Snaith, G. Hodes, D. Cahen, Interface-Dependent Ion Migration/Accumulation Controls Hysteresis in MAPbI3 Solar Cells, J. Phys. Chem. C 120 (30) (2016) 16399–16411.

[28] C. Ran, J. Xu, W. Gao, C. Huang, S. Dou, Defects in metal triiodide perovskite materials towards high-performance solar cells: origin, impact, characterization, and engineering, Chem. Soc. Rev. 47 (2018) 4581–4610, https://doi.org/10.1039/C7CS00868F.

[29] J. Lian, D. Lu, F. Niu, P. Zeng, X. Zhan, Electron-transport materials in perovskite solar cells, Small Methods 2 (2018) 1800082, https://doi.org/10.1002/smtd.201800082.

[30] D.H. Kim, G.S. Han, W.M. Seong, J.-W. Lee, B.J. Kim, N.-G. Park, K.S. Hong, S. Lee, H.S. Jung, Niobium doping effects on TiO2 mesoscopic electron transport layer-based perovskite solar cells, ChemSusChem 8 (14) (2015) 2392–2398.

[31] Y. Zhao, H. Zhang, X. Ren, H.L. Zhu, Z. Huang, F. Ye, D. Ouyang, K.W. Cheah, A.-Y. Jen, W.C.H. Choy, Thick TiO2-based top electron transport layer on perovskite for highly efficient and stable solar cells, ACS Energy Lett. 3 (12) (2018) 2891–2898.

[32] H.-H. Wang, Q.i. Chen, H. Zhou, L. Song, Z.S. Louis, N.D. Marco, Y. Fang, P. Sun, T.-B. Song, H. Chen, Y. Yang, Improving the TiO2 electron transport layer in perovskite solar cells using acetylacetonate-based additives, J. Mater. Chem. A 3 (17) (2015) 9108–9115.

[33] G. Tumen-Ulzii, T. Matsushima, D. Klotz, M.R. Leyden, P. Wang, C. Qin, J.-W. Lee, S.-J. Lee, Y. Yang, C. Adachi, Hysteresis-less and stable perovskite solar cells with a self-assembled monolayer, Commun. Mater. 1 (1) (2020), https://doi.org/10.1038/s43246-020-0028-z.

[34] T. Hu, S. Xiao, H. Yang, L. Chen, Y. Chen, Cerium oxide as an efficient electron extraction layer for p–i–n structured perovskite solar cells, Chem. Commun. 54 (2018) 471–474, https://doi.org/10.1039/C7CC08657A.

[35] R. Fang, S. Wu, W. Chen, Z. Liu, S. Zhang, R. Chen, Y. Yue, L. Deng, Y.-B. Cheng, L. Han, W. Chen, [6,6]-Phenyl-C61-butyric acid methyl ester/cerium oxide bilayer structure as efficient and stable electron transport layer for inverted perovskite solar cells, ACS Nano 12 (3) (2018) 2403–2414.

[36] K. Mahmood, B. S. Swain, A. Amassian, Double-layered ZnO nanostructures for efficient perovskite solar cells, Nanoscale 6 (24) (2014) 14674–14678.

[37] L. Xiong, Y. Guo, J. Wen, H. Liu, G. Yang, P. Qin, et al., Review on the application of SnO2 in perovskite solar cells, Adv. Funct. Mater. 28 (2018) 1802757, https://doi.org/10.1002/adfm.201802757.

[38] L. Zhu, Z. Shao, J. Ye, X. Zhang, X. Pan, S. Dai, Mesoporous BaSnO3 layer based perovskite solar cells, Chem. Commun. 52 (2016) 970–973, https://doi.org/10.1039/C5CC08156D.

[39] A. Roy, P. Selvaraj, P. Sujatha Devi, S. Sundaram, Morphology tuned BaSnO3 active layer for ambient perovskite solar cells, Mater. Lett. 219 (2018) 166–169, https://doi.org/10.1016/j.matlet.2018.02.055.

[40] M.d. Shahiduzzaman, A. Kulkarni, S. Visal, LiangLe Wang, M. Nakano, M. Karakawa, K. Takahashi, S. Umezu, A. Masuda, S. Iwamori, M. Isomura, T. Miyasaka, K. Tomita, T. Taima, A single-phase brookite TiO2 nanoparticle bridge enhances the stability of perovskite solar cells, Sustain. Energy Fuels 4 (4) (2020) 2009–2017.

[41] K. Dutta, S. De, B. Das, S. Bera, B. Guria, M.S. Ali, D. Chattopadhyay, Development of an efficient immunosensing platform by exploring single-walled carbon nanohorns (SWCNHs) and nitrogen doped graphene quantum Dot (N-GQD) nanocomposite for early detection of cancer biomarker, ACS Biomater. Sci. Eng. 7 (12) (2021) 5541–5554.

[42] M.S. Sheikh, A. Roy, S. Bhandari, T.K. Mallick, S. Sundaram, T.P. Sinha, Highly conductive double perovskite oxides A2LuTaO6 (A = Ba, Sr, Ca) as promising photoanode material for dye sensitized solar cells, Mater. Lett. 276 (2020), 128220, https://doi.org/10.1016/j.matlet.2020.128220.

[43] L. Giordano, G. Pacchioni, Oxide films at the nanoscale: new structures, new functions, and new materials, Acc. Chem. Res. 44 (2011) 1244–1252, https://doi.org/10.1021/ar200139y.

[44] A. Mamakhel, J. Yu, F. Søndergaard-Pedersen, P. Hald, B.B. Iversen, Facile synthesis of brookite TiO2 nanoparticles, Chem. Commun. 56 (2020) 15084–15087, https://doi.org/10.1039/D0CC06795D.

[45] M.d. Shahiduzzaman, S. Visal, M. Kuniyoshi, T. Kaneko, S. Umezu, T. Katsumata, S. Iwamori, M. Kakihana, T. Taima, M. Isomura, K. Tomita, Low-temperature-processed brookite-based TiO2 heterophase junction enhances performance of planar perovskite hole cells, Nano Lett. 19 (1) (2019) 598–604.

[46] C. Sun, L. Guan, Y. Guo, B. Fang, J. Yang, H. Duan, Y. Chen, H. Li, H. Liu, Ternary oxide BaSnO3 nanoparticles as an efficient electron-transporting layer for planar perovskite solar cells, J. Alloy. Compd. 722 (2017) 196–206.

[47] A. Roy, P.P. Das, P. Selvaraj, S. Sundaram, P.S. Devi, Perforated BaSnO3 nanorods exhibiting enhanced efficiency in dye sensitized solar cells, ACS Sustain Chem Eng 6 (2018) 3299–3310, https://doi.org/10.1021/acssuschemeng.7b03479.

[48] S. Bhandari, A. Roy, T.K. Mallick, S. Sundaram, Impact of different light induced effect on organic hole-transporting layer in perovskite solar cells, Mater. Lett. 268 (2020), 127568, https://doi.org/10.1016/j.matlet.2020.127568.

[49] S. Bhandari, A. Roy, A. Ghosh, T.K. Mallick, S. Sundaram, Performance of WO3-incorporated carbon electrodes for ambient mesoscopic perovskite solar cells, ACS Omega 5 (2020) 422–429, https://doi.org/10.1021/acsomega.9b02934.

[50] T.N. Stanislavchuk, A.A. Sirenko, A.P. Litvinchuk, X. Luo, S.-W. Cheong, Electronic band structure and optical phonons of BaSnO3 and Ba0.97La0.03SnO3 single crystals: theory and experiment, J. Appl. Phys. 112 (4) (2012) 044108.

[51] A. Roy, S. Bhandari, A. Ghosh, S. Sundaram, T.K. Mallick, Incorporating solution-processed mesoporous wo3 as an interfacial cathode buffer layer for photovoltaic applications, J. Phys. Chem. A 124 (2020) 5709–5719, https://doi.org/10.1021/acs.jpca.0c02912.

[52] A. Roy, P.P. Das, P. Selvaraj, P.S. Devi, S. Sundaram, Template free synthesis of CdSnO3 micro-cuboids for dye sensitized solar cells, J. Photochem. Photobiol. A Chem. 380 (2019), 111824, https://doi.org/10.1016/j.jphotochem.2019.04.035.

[53] L. Zhu, J. Ye, X. Zhang, H. Zheng, G. Liu, X.u. Pan, S. Dai, Performance enhancement of perovskite solar cells using a La-doped BaSnO3 electron transport layer, J. Mater. Chem. A 5 (7) (2017) 3675–3682.

[54] S.D. Stranks, G.E. Eperon, G. Grancini, C. Menelaou, M.J.P. Alcocer, T. Leijtens, L.M. Herz, A. Petrozza, H.J. Snaith, Electron-hole diffusion lengths exceeding 1 micrometer in an organometal trihalide perovskite absorber, Science (80-) 342 (6156) (2013) 341–344.

[55] Z. Yang, Z. Yu, H. Wei, X. Xiao, Z. Ni, B.o. Chen, Y. Deng, S.N. Habisreutinger, X. Chen, K. Wang, J. Zhao, P.N. Rudd, J.J. Berry, M.C. Beard, J. Huang, Enhancing electron diffusion length in narrow-bandgap perovskites for efficient monolithic perovskite tandem solar cells, Nat. Commun. 10 (1) (2019), https://doi.org/10.1038/s41467-019-12513-x.

[56] S. Nundy, D. Tatar, J. Kojčinović, H. Ullah, A. Ghosh, T.K. Mallick, et al. Bandgap Engineering in Novel Fluorite-Type Rare Earth High-Entropy Oxides (RE-HEOs) with Computational and Experimental Validation for Photocatalytic Water Splitting Applications. Adv Sustain Syst 2022;n/a:2200067. 10.1002/adsu.202200067.

[57] W. Hao, Q. He, K. Zhou, G. Xu, W. Xiong, X. Zhou, et al. Low defect density and small I − V curve hysteresis in NiO/β-Ga2O3 pn diode with a high PFOM of 0.65 GW/cm2. Appl Phys Lett 2021;118:43501. https://doi.org/10.1063/5.0038349.

[58] Q.i. Wang, B.o. Chen, Y.e. Liu, Y. Deng, Y. Bai, Q. Dong, J. Huang, Scaling behavior of moisture-induced grain degradation in polycrystalline hybrid perovskite thin films, Energy Environ. Sci. 10 (2) (2017) 516–522.

[59] B.P. Uberuaga, L.J. Vernon, E. Martinez, A.F. Voter, The relationship between grain boundary structure, defect mobility and grain boundary sink efficiency, Sci. Rep. 5 (2015) 9095, https://doi.org/10.1038/srep09095.

[60] Y. Yang, K. Ri, A. Mei, L. Liu, M. Hu, T. Liu, X. Li, H. Han, The size effect of TiO2 nanoparticles on a printable mesoscopic perovskite solar cell, J. Mater. Chem. A 3 (17) (2015) 9103–9107.

[61] Q. Guo, J. Wu, Y. Yang, X. Liu, W. Sun, Y. Wei, Z. Lan, J. Lin, M. Huang, H. Chen, Y. Huang, Low-temperature processed rare-earth doped brookite TiO2 scaffold for UV stable, hysteresis-free and high-performance perovskite solar cells, Nano Energy 77 (2020) 105183, https://doi.org/10.1016/j.nanoen.2020.105183.

[62] V. Sugathan, E. John, K. Sudhakar, Recent improvements in dye sensitized solar cells: a review, Renew. Sustain. Energy Rev. 52 (2015) 54–64, https://doi.org/10.1016/j.rser.2015.07.076.

[63] B. Conings, J. Drijkoningen, N. Gauquelin, A. Babayigit, J. D'Haen, L. D'Olieslaeger, A. Ethirajan, J.o. Verbeeck, J. Manca, E. Mosconi, F.D. Angelis, H.-G. Boyen, Intrinsic thermal instability of methylammonium lead trihalide perovskite, Adv. Energy Mater. 5 (15) (2015) 1500477.

[64] T. Leijtens, G.E. Eperon, S. Pathak, A. Abate, M.M. Lee, H.J. Snaith, Overcoming ultraviolet light instability of sensitized TiO2 with meso-superstructured organometal tri-halide perovskite solar cells, Nat. Commun. 4 (2013) 2885, https://doi.org/10.1038/ncomms3885.

[65] I. Mesquita, L. Andrade, A. Mendes, Temperature impact on perovskite solar cells under operation, ChemSusChem 12 (2019) 2186–2194, https://doi.org/10.1002/cssc.201802899.